Journal of Electronic Materials (2024) 53:2382–2397
https://doi.org/10.1007/s11664-024-10973-6

ORIGINAL RESEARCH ARTICLE

Investigation of the Influence of Au (Gold) Doping Concentration on the Structural, Morphological, Optical, and Electrical Parameters of an Al/Au:CuO/n-Si Heterojunction Device

Halit Cavusoglu[1,2] · Ali Akbar Hussaini[3] · Huseyin Sakalak[2,4] · Adem Koçyiğit[5] · Fatih Durmaz[6] · Murat Yıldırım[3]

Received: 6 September 2023 / Accepted: 26 January 2024 / Published online: 29 February 2024

Abstract

In this investigation, we achieved successful deposition of nanostructured cupric oxide (CuO) thin films onto glass substrates through implementation of successive ionic layer adsorption and reaction (SILAR), all carried out at room temperature. This approach has proven to be highly efficient and yielded favorable results in terms of film quality and uniformity. A comprehensive investigation was conducted to analyze the effect of gold (Au) on the structural, morphological, optical, and electrical properties of nanocrystalline CuO thin films. The structural analysis confirmed that the films were polycrystalline, exhibiting a monoclinic crystal structure with preferential orientations along the $(\bar{1}11)$ and (111) planes. The estimated crystallite sizes ranged from 20.37 to 30.77 nm, indicating the nanoscale nature of the films. Scanning electron microscopy/energy-dispersive x-ray analysis (SEM/EDX) was executed to reveal the Au dopant on the surface of CuO thin films. Surface analysis revealed the presence of uniformly dispersed CuO nanostructures across the film surfaces. Through optical investigations, it was observed that the bandgap energy of the CuO thin films decreased from 1.52 to 1.45 eV with increasing Au concentration. Furthermore, the average transmittance of the films exhibited a decrease from 4.9% to 1.3% as the Au concentration increased. The electrical properties of the Al/Au:CuO/n-Si heterojunction were studied using current–voltage (*I–V*) measurements for various light power densities. The Al/Au:CuO/n-Si heterojunction exhibited good photodiode behavior, with 3.44 A/W responsivity and 1.58×10^{10} Jones specific detectivity for the 2% Au-doped CuO interfacial layer.

Keywords SILAR · CuO thin film · electrical characteristics · heterojunction · Au

✉ Halit Cavusoglu
hcavusoglu@selcuk.edu.tr

✉ Adem Koçyiğit
adem.kocyigit@bilecik.edu.tr

✉ Murat Yıldırım
muratyildirim@selcuk.edu.tr

[1] Department of Physics, Faculty of Sciences, Selcuk University, 42130 Konya, Turkey

[2] Advanced Nanotechnology Research Laboratory, Faculty of Science, Selcuk University, 42130 Konya, Turkey

[3] Department of Biotechnology, Faculty of Sciences, Selcuk University, 42130 Konya, Turkey

[4] Graduate School of Natural and Applied Sciences, Nanotechnology and Advanced Materials, Selcuk University, 42130 Konya, Selcuklu, Turkey

[5] Vocational High School, Department of Electronic and Automation, Bilecik Seyh Edebali University, 11230 Bilecik, Turkey

[6] Department of Chemistry, Faculty of Sciences, Selcuk University, 42130 Konya, Turkey

Introduction

In recent years, optoelectronic devices such as laser diodes, solar cells, light-emitting diodes (LEDs), and photosensors have played a significant role in human life. Among these devices, photosensors are particularly attractive, as they can convert optical signals into electrical signals. There are various types of photosensors available for different applications, including photodiodes, UV photodetectors, photoresistors, and phototransistors. Photosensors can be classified into two main types based on their device structure: metal–semiconductor–metal (MSM) and heterojunction photodetectors. Considering previously published reports, the p–n junction photodetector is more efficient than MSM photodetectors, as it generates electron–hole pairs through the internal electric field in its depletion region.[1] The choice of materials for photodetectors depends on their intended application in the electromagnetic spectrum, such as the ultraviolet (UV), visible, or infrared (IR) regions.

For the fabrication of a heterojunction photodiode, the material must have a high absorption coefficient, a suitable energy bandgap, and good electrical conductivity.[2] Metal oxide-based materials are considered prominent candidates for heterojunction photodiode production, from a technological and scientific perspective. These materials include magnesium oxide (MgO), aluminum oxide (Al_2O_3), zinc oxide (ZnO), cadmium oxide (CdO), nickel oxide (NiO), and cupric oxide (CuO).[3–8] CuO stands out among these oxides for its remarkable multifunctional properties, encompassing magnetic, semiconducting, and optoelectronic functionalities.[9–11] CuO exhibits fascinating characteristics as a p-type semiconductor, displaying a high absorption coefficient (~1.2×10^5 cm^{-1}) and a low bandgap (~1.4–2.1 eV).[12] This compound holds significant appeal due to its affordability, exceptional reactivity, and nontoxic nature.[13]

As a result, CuO finds extensive utility in diverse electrical components such as solar cells, gas sensors, Li batteries, and catalysts. Its versatile application across these fields showcases the broad spectrum of benefits offered by CuO.[14–18]

Currently, a wide range of physical and chemical deposition processes are being used to fabricate copper oxide (CuO) thin films. Upon careful examination, it has been established that chemical deposition methods offer superior economic feasibility and practicality compared to their physical counterparts. Several techniques have been employed for the deposition of CuO thin films, including spin coating generated from sol–gel,[19] spray pyrolysis,[20] microwave-assisted hydrothermal synthesis,[21] electrochemical deposition,[22] chemical bath deposition (CBD),[23] and successive ionic layer adsorption and reaction (SILAR).[24] Notably, SILAR stands out among these chemical deposition methods due to its straightforward solution-based approach, allowing for precise control over film thickness and deposition at low temperatures.

The scientific community widely recognizes the existence of various strategies for manipulating the physical and optical properties of thin films fabricated through solution phase deposition techniques.[25] One such strategy involves incorporating dopant materials into the growth solution.[26] Dopant incorporation plays a pivotal role in determining the physical attributes and potential applications of different materials, particularly semiconductors.[27] Throughout the deposition process of CuO thin films, several dopants, including Ni, Ce, Ag, and Co, have been extensively explored.[28–31] Consequently, it is reasonable to explore the effects of Au doping as it holds the potential to enhance multiple characteristics of CuO-based materials.

Considering the aforementioned factors, numerous researchers remain actively involved in endeavors to further enhance the diverse properties of CuO-based semiconductor materials. To the best of our knowledge, no other authors have yet investigated the impact of Au doping on CuO thin films synthesized through SILAR. Therefore, our study aims to fill this gap in the literature and contribute to a more comprehensive understanding of the potential benefits of Au doping for CuO-based materials.

The objective of this study is to utilize the SILAR technique for the fabrication of Al/Au:CuO/n-Si heterojunction structures, while examining how the growth strategy affects the crystallographic structure, shape, optical properties, and electrical properties.

Experimental Section

Thin Film Growth Procedure

Nanocrystalline CuO thin films were synthesized on pre-cleaned soda lime glass substrates using SILAR, with varying concentrations of Au. In this process, an aqueous copper–ammonia ion complex ($[Cu(NH_3)_4]^{2+}$) was utilized for the cationic precursor solution. A suitable amount of $CuCl_2{\cdot}2H_2O$, a highly pure cupric chloride dihydrate purchased from Sigma Aldrich, and 25% aqueous ammonia solution from Merck were carefully added in appropriate proportions to form the precursor solution. $CuCl_2{\cdot}2H_2O$ was used to reduce the concentration of the copper(II) chloride solution to 0.1 M while maintaining a 1:10 molar ratio of copper to NH_3. Reaction temperature was maintained at 90 °C during the entire process. The anionic precursor solution consisted of hot deionized water at the same temperature. CuO thin films were synthesized by immersing glass substrates consecutively in the $[Cu(NH_3)_4]^{2+}$ combination and the precursor anionic solution. The prepared solution was applied to the substrates vertically and left on for 20 s, and this dipping process was repeated for a total of 15 cycles. In order to investigate the impact of Au as a dopant, different concentrations of Au (1.0 M%, 2.0 M%, and 4.0 M%) were incorporated into the growth solutions. Au acts as a chelating agent associating with copper ions to facilitate the formation of CuO thin films. As a result, the Cu^{2+} and O^{2-} ions in the solution were released under control, leading to their condensation onto the glass substrates and ultimately resulting in the formation of CuO thin films. To prepare the samples for characterization, they were annealed for 2 h at 400 °C under an air atmosphere.

Thin Film Characterization

The surface morphology and elemental composition of the deposited thin films were investigated using a Zeiss EVO LS 10 scanning electron microscope (SEM, Carl Zeiss NTS GmbH, Oberkochen, Germany) equipped with an

energy-dispersive x-ray spectroscopy (EDX) system. For the characterization of the microstructure of the deposited thin films, x-ray diffraction (XRD) was carried out using a Bruker D8 Advance diffractometer (XRD, Bruker AXS GmbH) equipped with Cu-Kα radiation (wavelength λ = 1.5418 Å). The diffraction angles were selected within the range of 30° to 70°. The thickness of the CuO thin films with different Au concentrations was determined using the NanoMap-500LS contact surface profilometer . The UV–Vis absorption and transmission spectra of the thin films were obtained over the wavelength range of 190–1100 nm using a UV–Vis–near-infrared (NIR) spectrophotometer (Jasco Inc., MD, USA). A Keithley 6487 picoammeter/voltage source (Keithley Instruments, Cleveland, OH, USA) was used to test the electrical conductivity and resistivity of all deposited layers.

Fabrication and Measurements of the Al/Au:CuO/*n*-Si Heterostructure

An *n*-type Si wafer with a carrier concentration of 7.3×10^{15} cm^{-3}, polished on one side and oriented in the (111) direction, was employed in the fabrication of the Al/Au:CuO/*n*-Si heterostructures. The *n*-type Si wafer was sliced into 1×2 cm^2 pieces and then cleaned by ultrasonication in isopropanol, acetone, and deionized water solvents. To remove the undesired oxide layer, the pieces were dipped into HF:H_2O (1:10) solution for 30 s after cleaning. A thermal evaporator was used to deposit aluminum to obtain an ohmic contact of 150 nm on the back surfaces of the Si wafer pieces, followed by annealing in N_2 medium for 5 min in an oven. After deposition of Au:CuO films on the polished surface of the pieces, Au:CuO/*n*-Si structures were again immediately transferred into the thermal evaporator to obtain 1-mm-diameter Al metallic contacts of 100 nm on the top of the Au:CuO film layer by a hole array mask. Thus, fabrication of the Al/Au:CuO/*n*-Si heterostructures was completed. Current–voltage (*I–V*) and *I–t* measurements were obtained by a Fytronix FY-7000 solar simulator measurement system under various power densities from 20 to 100 mW/cm^2 at room temperature for a voltage range of ± 5 V by a 1.5 AM filter.

Results and Discussion

Structural Evaluation

X-ray diffraction (XRD) measurements were performed to examine the structural properties of both Au-doped and undoped CuO thin films. The XRD parameters were employed to estimate crystallite size, peak intensity, texture coefficient, and microstrain. Figure 1a presents the XRD patterns for CuO samples with and without Au, providing a comprehensive depiction of their structural features. The XRD analysis revealed that all the deposited CuO thin films possessed a distinct crystalline structure, exhibiting diffractograms consistent with the monoclinic phase of CuO (JCPDS file No. 01-080-0076). Analysis of the XRD patterns in Fig. 1a reveals a preferential growth of CuO thin films along the $\left(\bar{1}11\right)$ and (111) crystallographic planes, as evidenced by the prominence of two dominant peaks (2θ = 35.64°, 38.78°). In addition to the two primary peaks, six additional diffraction lines corresponding to the (110), $(\bar{2}02)$, (020), $(\bar{1}13)$, $(\bar{3}11)$, and (220) crystallographic planes were identified. No supplementary peaks indicative of other CuO phases were detected. The observed relative peak intensity values of Au-doped and undoped CuO thin films corresponding to the (110), $\left(\bar{1}11\right)$, (111), and $(\bar{2}02)$ planes are displayed in Fig. 1b and Table I. According to Table I and Fig. 1b, it can be observed that the intensities of the $(\bar{1}11)$ and (111) peaks increased proportionally with the Au content, indicating enhanced preferential growth in these crystallographic planes. Similarly, other XRD peaks such as (110), $(\bar{2}02)$, (020), $(\bar{1}13)$, $(\bar{3}11)$, and (220) also exhibited similar increases upon Au doping. These changes are likely attributable to the internal strain induced by the presence of Au. These findings suggest the potential preferential orientation of CuO thin films, which can be attributed to their anisotropic crystallographic characteristics.

The texture coefficient ($TC_{(hkl)}$) is a quantitative measure that indicates the degree of orientation preference of crystal planes within the CuO film. ($TC_{(hkl)}$) values are used to assess the dominant growth orientation in each CuO sample. The coefficient values for the different crystallographic planes are provided according to the following relationship[32];

$$TC_{(hkl)} = \frac{I_{(hkl)} / I_{0(hkl)}}{N^{-1} \sum_{N} I_{(hkl)} / I_{0(hkl)}} \quad (1)$$

the texture coefficient $TC_{(hkl)}$ is determined based on the measured peak intensity $I_{(hkl)}$ and the standard reference intensity values $I_{0(hkl)}$ taken from JCPDS card no. 01-080-0076.

The $TC_{(hkl)}$ for various crystallographic planes are presented in Fig. 1c and given in Table I. Variations in the $TC_{(hkl)}$ values were observed in CuO thin films with different Au concentrations.

To examine the impact of Au doping at various concentrations on the microstructural characteristics, the crystallite size (*D*) and microstrain (*ε*) of the CuO thin films was determined using the XRD data and the following equations[32];

$$D = \frac{0.94\lambda}{\beta \cos\theta} \quad (2)$$

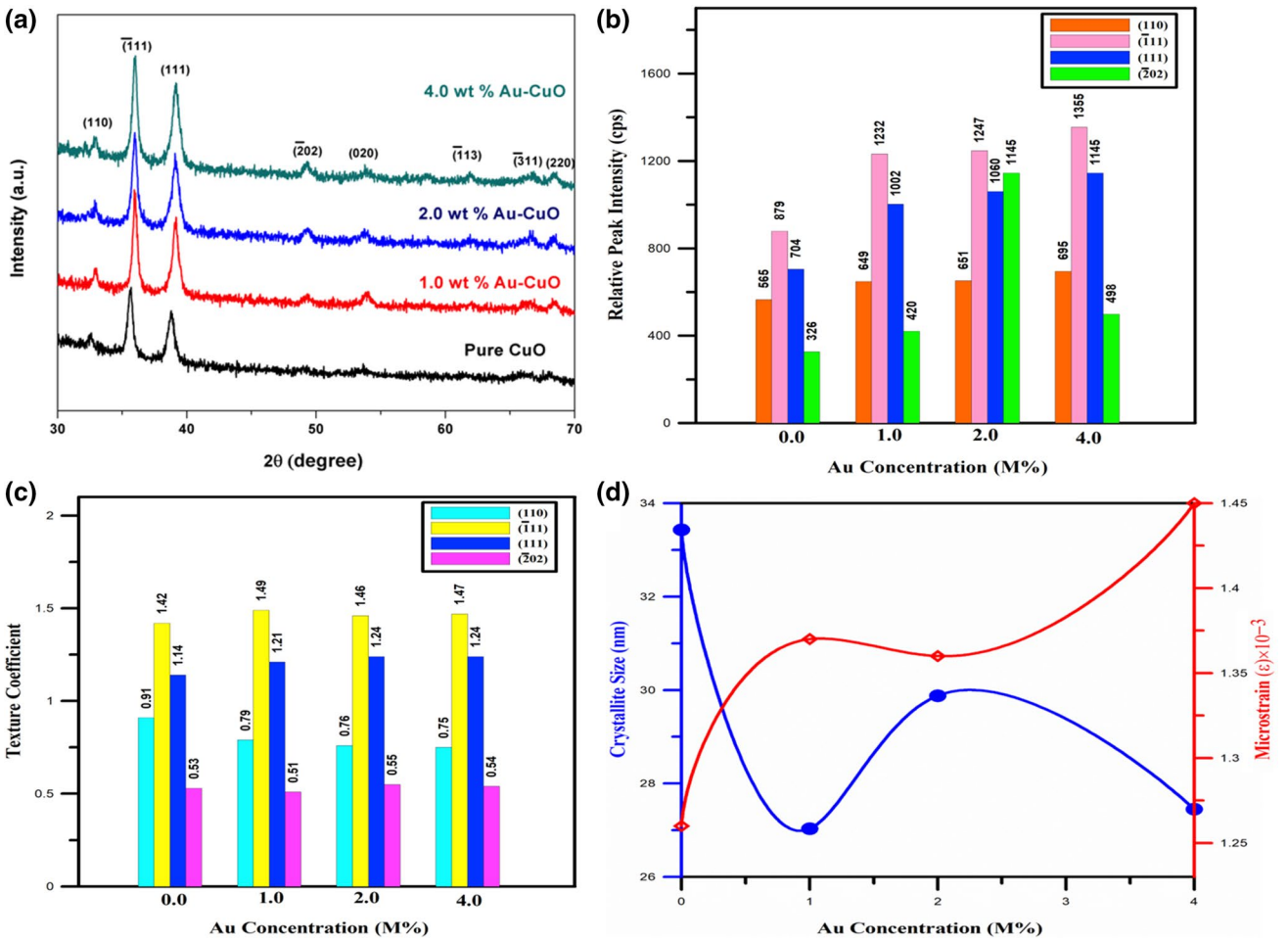

Fig. 1 XRD patterns of Au-doped CuO thin films (a). The relative peak intensity values for (110), $(\bar{1}11)$, (111), and $(\bar{2}20)$ planes of CuO thin films as a function of Au concentration (b). The texture coefficient for (110), $(\bar{1}11)$, (111), and $(\bar{2}20)$ planes of CuO thin films in relation to different Au concentrations (c). The relationship between the crystallite size and microstrain of CuO thin films in relation to different Au concentrations (d).

Table I The relative peak intensities and $TC_{(hkl)}$ values of CuO thin films were examined in relation to different Au concentrations using XRD analysis

Au Concentration, M%	Recorded peak intensity		TC, $_{hkl}$			
	$(\bar{1}11)$	(111)	(110)	$(\bar{1}11)$	(111)	$(\bar{2}02)$
0	879	704	0.91	1.42	1.14	0.53
1.00	1232	1002	0.79	1.49	1.21	0.51
2.00	1247	1060	0.76	1.46	1.24	0.55
4.00	1355	1145	0.75	1.47	1.24	0.54

and

$$\varepsilon = \frac{\beta \cos\theta}{4} \tag{3}$$

where θ is the Bragg diffraction angle, β is the full width at half-maximum (FWHM) value of the peak, and λ is the x-ray wavelength. The XRD measurements provided the mean crystallite size and microstrain values for CuO samples with varying concentrations of Au doping. The FWHM of the peak, Bragg's diffraction angle (θ), and the x-ray wavelength (λ) were used to determine the crystallite size. The results are presented in Table II. It was noted that increasing

the Au concentration caused the crystallite size of the CuO samples to grow. Figure 1d depicts the variation of crystallite size and microstrain with Au solution concentration. It can be seen from Fig. 1d and Table II that the crystallite size exhibited a decrease from 33.43 nm to 27.45 nm, whereas the microstrain demonstrated an increase from 1.26×10^{-3} to 1.45×10^{-3} with an increase in the concentration of Au in the reaction mixture. In other words, Fig. 1d illustrates a reverse relationship between the microstrain and crystallite size values of the CuO thin films in relation to different Au concentrations. Other researchers have observed similar findings[33,34] in the literature.

Table II The dependence of CuO thin film properties, including crystallite size, microstrain, film thickness, and optical bandgap, on varying concentrations of Au doping

Au concentration, M%	Crystallite size, nm	Microstrain, $\varepsilon\times10^{-3}$	Film thickness, nm	Optical bandgap, eV
0	33.43	1.26	852	1.52
1.00	27.03	1.37	1327	1.47
2.00	29.88	1.36	1494	1.48
4.00	27.45	1.45	1612	1.45

Morphological Analysis of Thin Film Surfaces

SEM Analysis

The optical characteristics of CuO thin films are influenced by their surface properties, which are important for applications in optoelectronic devices. In order to investigate the impact of Au doping on the surface morphology of CuO thin films, SEM-EDX analysis was conducted. The SEM images in Fig. 2a, b, c, and d illustrate the morphology of CuO thin films with different molar concentrations of Au. The images clearly show that the CuO thin films adhere strongly to the glass substrate surface, with a considerable number of particles uniformly distributed across the entire surface area of the glass slide. The introduction of Au into the solution bath leads to changes in particle size and structure. Therefore, the morphological changes observed can be attributed to the

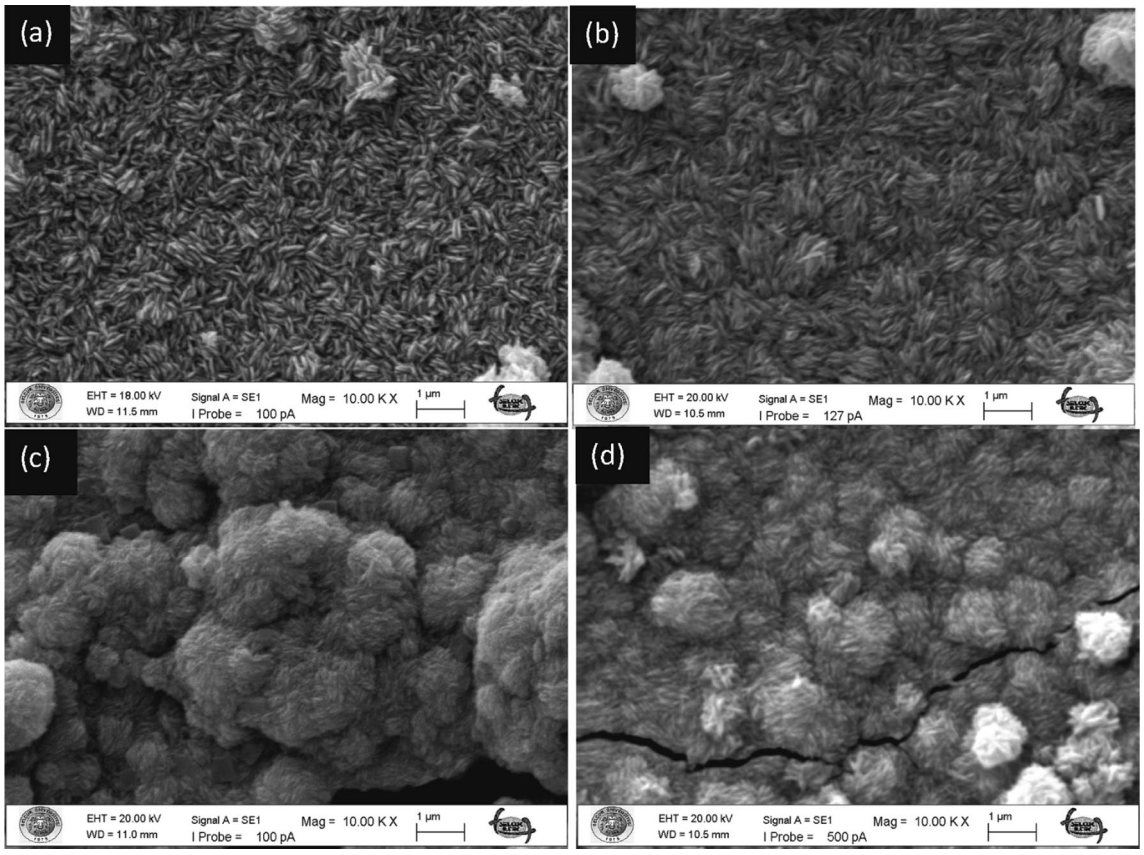

Fig. 2 SEM images obtained for CuO thin films doped with various molar concentrations of Au: (a) 0 M%, (b) 1.0 M%, (c) 2.0 M%, (d) 4.0 M%.

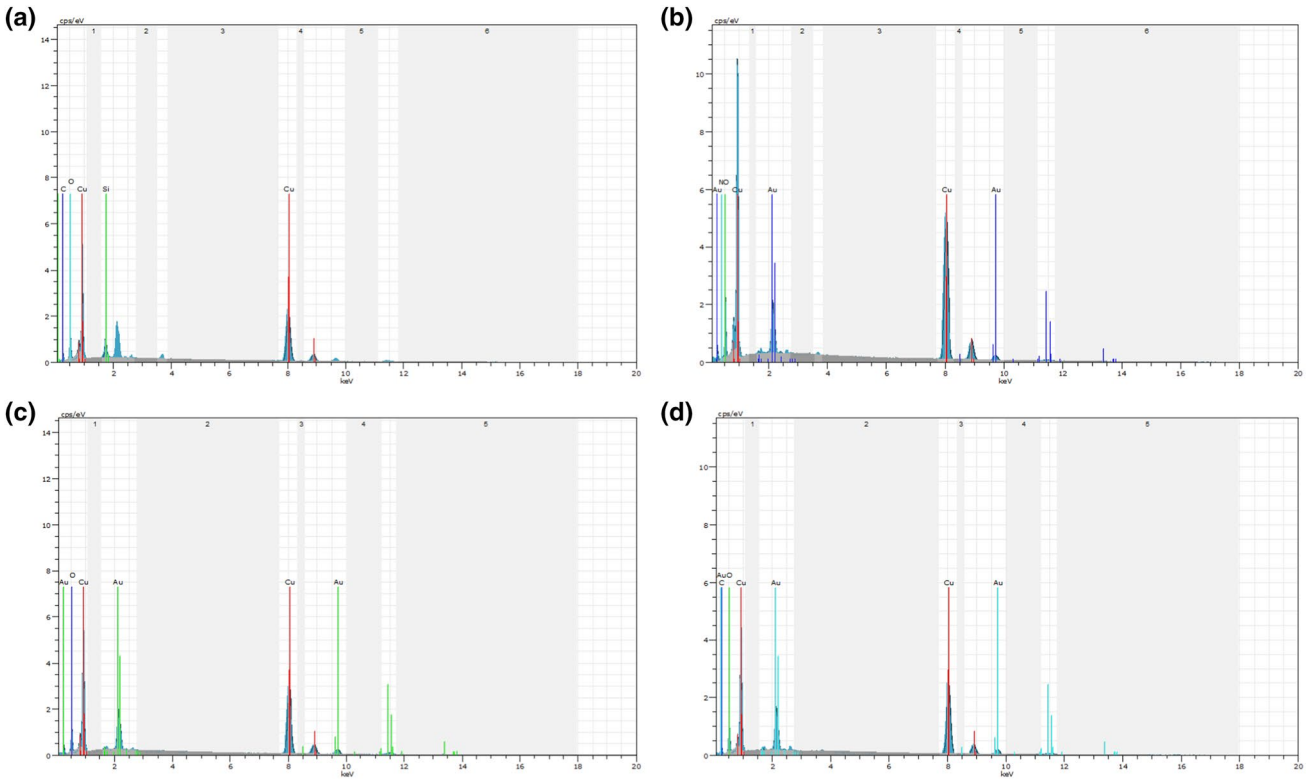

Fig. 3 EDX spectra of CuO thin films doped with Au at varying molar concentrations. (a) Undoped, (b) 1% Au doping, (c) 2% Au doping, and (d) 4% Au doping.

Table III Elemental analysis (reported as relative weight percentages, wt%) of CuO thin films doped with Au at varying molar concentrations (0 M%, 1.0 M%, 2.0 M%, 4.0 M%)

Au concentration, M%	Element	Series	Unn. C, wt.%	Norm. C, wt.%	Atom. C, at. %	Error, %
0	Copper	K-series	47.32	72.69	40.25	1.3
	Silicon	K-series	2.78	4.27	5.74	0.1
	Carbon	K-series	3.30	5.07	14.85	0.6
	Oxygen	K-series	11.70	17.98	39.55	1.8
1.00	Copper	K-series	70.80	73.49	59.72	1.9
	Gold	L-series	14.98	15.55	4.08	0.6
	Oxygen	K-series	9.78	10.15	32.76	1.4
	Carbon	K-series	0.77	0.80	3.45	0.3
2.00	Copper	K-series	72.83	70.47	67.26	2.1
	Gold	L-series	22.99	22.26	7.00	0.9
	Oxygen	K-series	7.02	6.79	23.49	1.3
	Carbon	K-series	0.51	0.48	2.25	0.3
4.00	Copper	K-series	72.91	67.49	65.77	2.1
	Gold	L-series	27.99	25.91	8.15	1.1
	Oxygen	K-series	6.66	6.17	23.87	1.3
	Carbon	K-series	0.46	0.43	2.21	0.3

unn. C [wt. %] is the unnormalised concentration in weight percent of the element

interaction between Cu^{2+} and Au throughout the synthesis procedure.[34,35]

The EDX spectra and elemental analysis of these deposited nanostructures are presented in Fig. 3 and tabulated in Table III. Figure 3 reveals the presence of Cu and O atoms

in the undoped CuO sample, with a proportional distribution of Cu (72.69%) and O (17.98%). When the other spectra are examined carefully, the Au concentration in the chemical composition clearly increases by weight with an increase in the ratio of Au doping. At 1% Au doping concentration, the sample contains 73.49% Cu, 10.15% O, and 15.55% Au. When the Au doping level reaches 2%, the chemical composition is 70.47% Cu, 6.79% O, and 22.26% AU. When the Au doping concentration is 4%, the maximum Au content (25.91%) in the chemical composition is reached.

Optical Evaluation

The optical properties of both Au-doped and undoped CuO thin films were analyzed using a UV–Vis spectrophotometer. The bandgap energies of these films were calculated using Eq. 4, where α is the absorption coefficient, ν is the frequency, E_g is the bandgap energy, m is the exponential constant ($m = ½$ for permitted direct transition), and C is the proportionality constant:

$$\alpha h\nu = C\left(h\nu - E_g\right)^m \tag{4}$$

To analyze the effect of Au concentration on the bandgap values, the graphs of $(\alpha h\nu)^2$ versus $(h\nu)$ were drawn in relation to different Au concentrations, as shown in Fig. 4a. The obtained optical energy values for all CuO thin films are also presented in Table II. Figure 4b demonstrates that the CuO thin films' energy values shown in Fig. 4b were determined as 1.52, 1.47, 1.48, and 1.45 eV for Au concentrations of 0 M%, 1.00 M%, 2.00 M%, and 4.00 M%, respectively.

The optical transmittance spectra of CuO thin films were measured at different Au concentrations (0, 1.0, 2.0, and 4.00 M%) within the spectral range of 400–1100 nm, as depicted in Fig. 4c. The CuO thin film without Au doping exhibited the highest transmittance, approximately 4.9%.

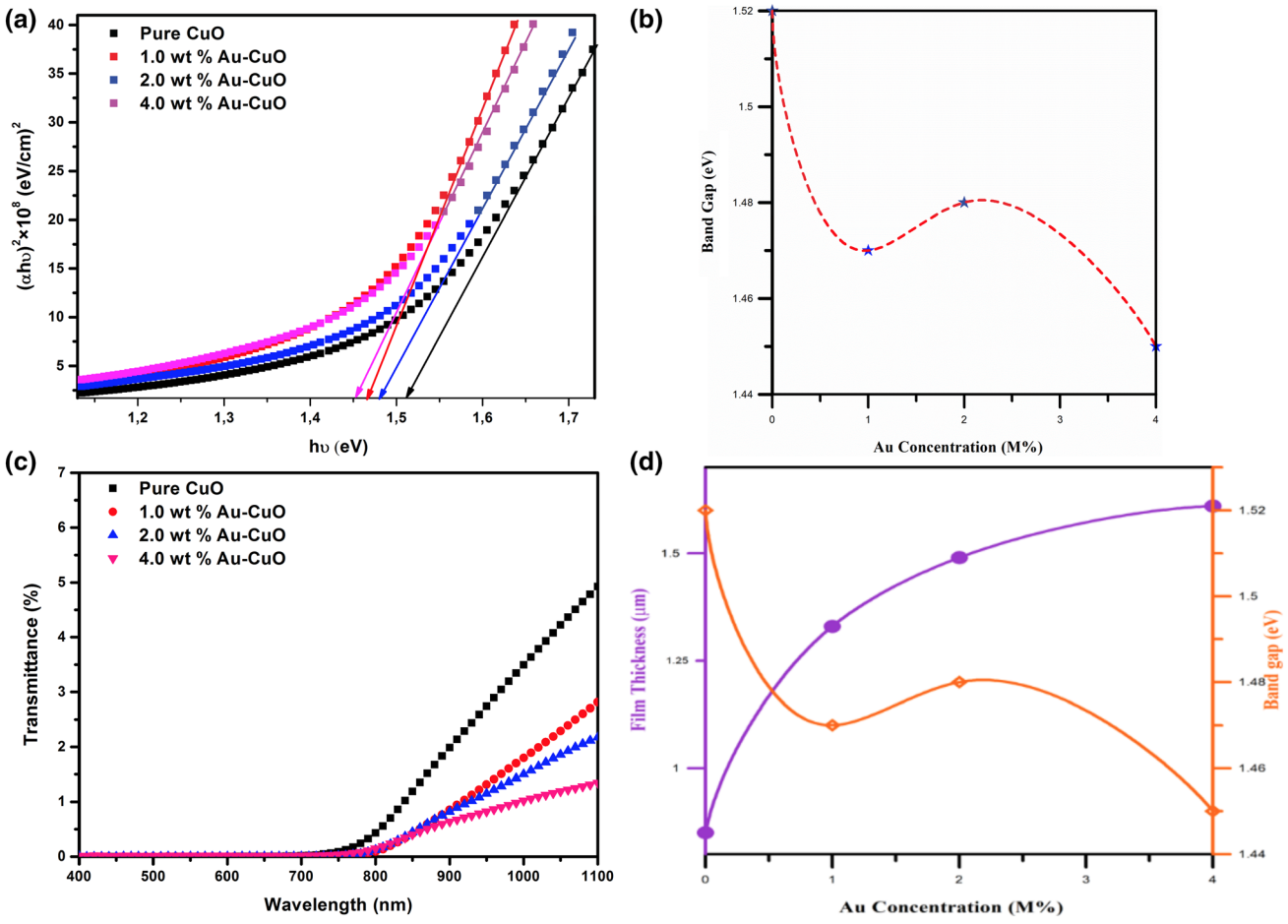

Fig. 4 CuO thin film bandgap energy values evaluated with various Au concentrations (a). The impact of doping on the bandgap of CuO thin films, comparing undoped films with Au-doped films (b). The transmittance spectra of CuO thin films measured at different Au concentrations (c). The variations in CuO thin film thickness and bandgap analyzed as a function of Au concentration (d).

However, as the Au content in the solution bath increased, the optical transmittance decreased rapidly, ranging from approximately 4.9%–1.3%. The maximum transmittance of around 4.9% was observed with a 4.0 M% Au concentration. CuO thin film transmittance values varied, and it was determined that this was because each film had a different thickness and degree of transparency.[36]

The thickness of the deposited thin films plays a crucial role in determining their physical characteristics, particularly their optical properties. To investigate this, the thickness of CuO thin films with different Au concentrations was measured using a contact surface profilometer. Table II presents the thickness values of all the deposited CuO thin films. The dependence of film thickness and bandgap on Au concentrations are demonstrated in Fig. 4d. It is observed that as the Au concentration increases, the film thickness increases while the bandgap values decrease. Specifically, the film thickness ranges from 0.85 µm (without Au) to 1.61 µm (for 4.0 M% Au in the growth solution), while the bandgap decreases rapidly from 1.52 eV to 1.45 eV. It is possible to attribute changes in the surface crystallinity and stresses present in the CuO films to the observed variations in film thickness and bandgap with increasing Au content.[37]

Electrical Analysis

The various Au-doped CuO thin films were used as interfacial material for the Al/Au:CuO/*n*-Si heterostructure to determine photodetection performance. The *I–V* characteristics of the various Au-doped CuO interlayered heterostructures have been given in Fig. 5 for various Au doping levels. The reverse current values were increased

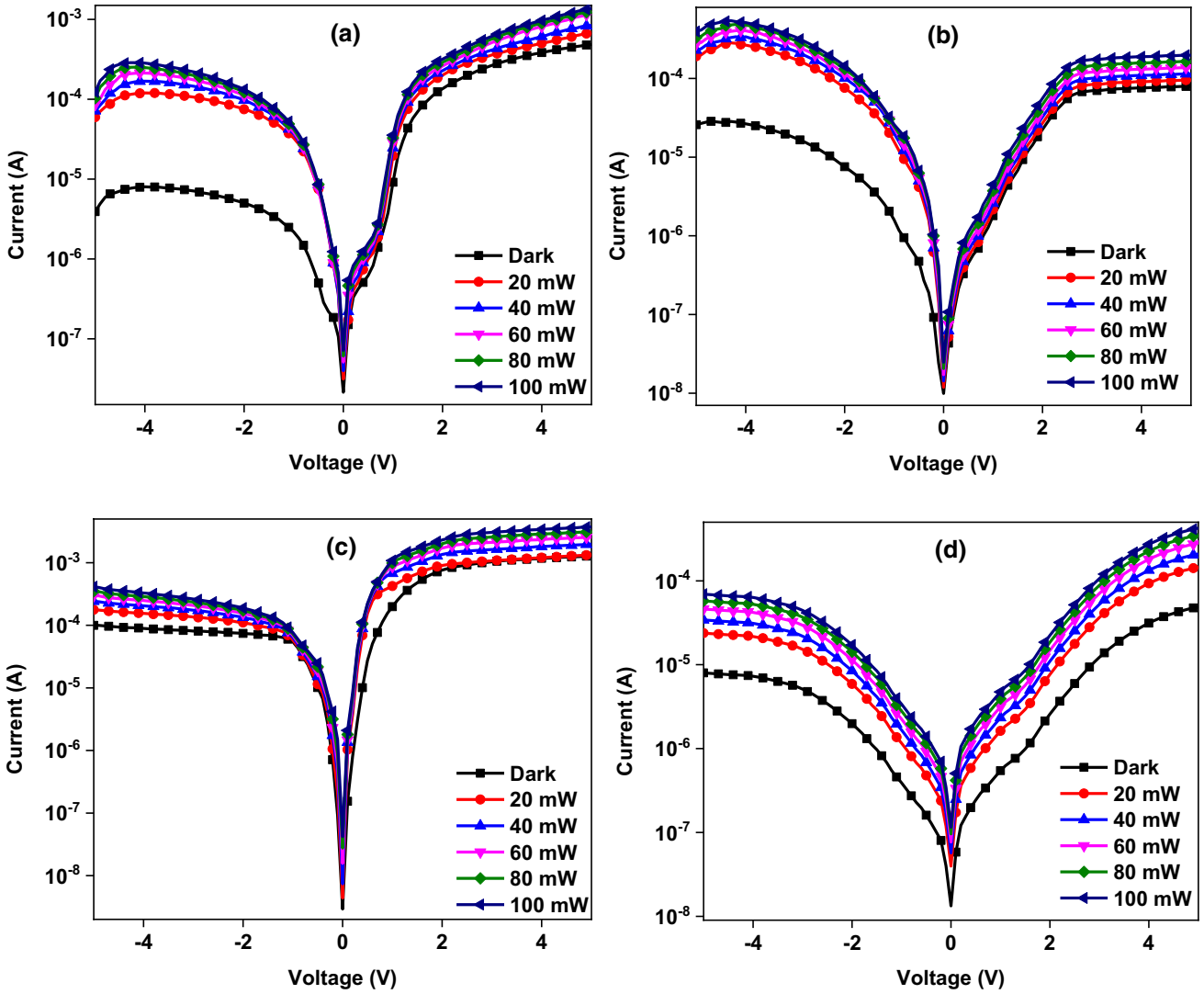

Fig. 5 *I–V* characteristics of the various Au-doped CuO interlayered Al/Au:CuO/*n*-Si heterostructures. (a) Undoped, (b) 1% Au doping, (c) 2% Au doping, and (d) 4% Au doping.

with increasing the Au doping level of 1% and 2% and decreased slightly for 4% at the dark condition measurements. Furthermore, the forward currents increased with increasing light power, but the highest increase were seen at the 4% Au-doped Al/Au:CuO/*n*-Si heterostructure. Au decorated heterostructures exhibited higher current values at reverse biases for 1% and %2 Au doping levels than undoped ones with increasing dark currents. However,

Table IV Diode parameters for various Au-doped CuO interlayered Al/Au:CuO/*n*-Si heterostructures for dark conditions

Au doping level	Saturation current, I_0	n, I–V -	n Cheung -	$\Phi_b(I$–$V)$, eV	Φ_b Cheung, eV	Φ_b Norde, eV	R_s Cheung, kΩ (H(I))	R_s Cheung, kΩ ($dV/d\ln(I)$)	R_s Norde, kΩ
0%	1.11×10^{-8}	5.95	4.43	0.77	0.77	0.72	6.78	6.69	3.91
1%	8.94×10^{-8}	14.32	11.96	0.71	0.72	0.76	7.48	7.86	4.01
2%	4.36×10^{-8}	3.00	3.24	0.73	0.72	0.79	1.58	2.55	2.51
4%	5.77×10^{-8}	20.27	18.10	0.72	0.73	0.72	28.44	29.62	155.86

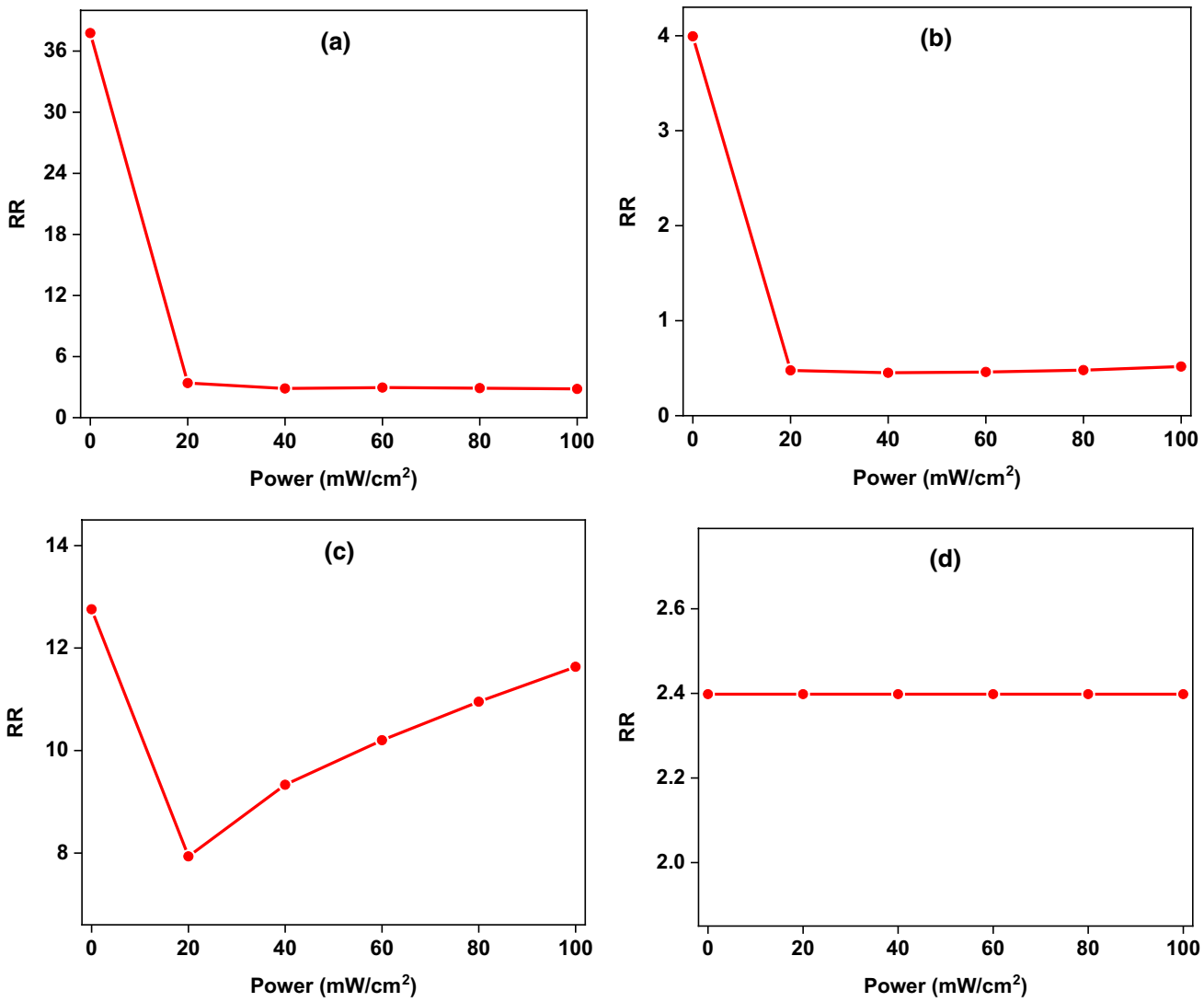

Fig. 6 *RR* plots of the various Au-doped CuO interlayered Al/Au:CuO/*n*-Si heterostructures. (a) Undoped, (b) 1% Au doping, (c) 2% Au doping, and (d) 4% Au doping.

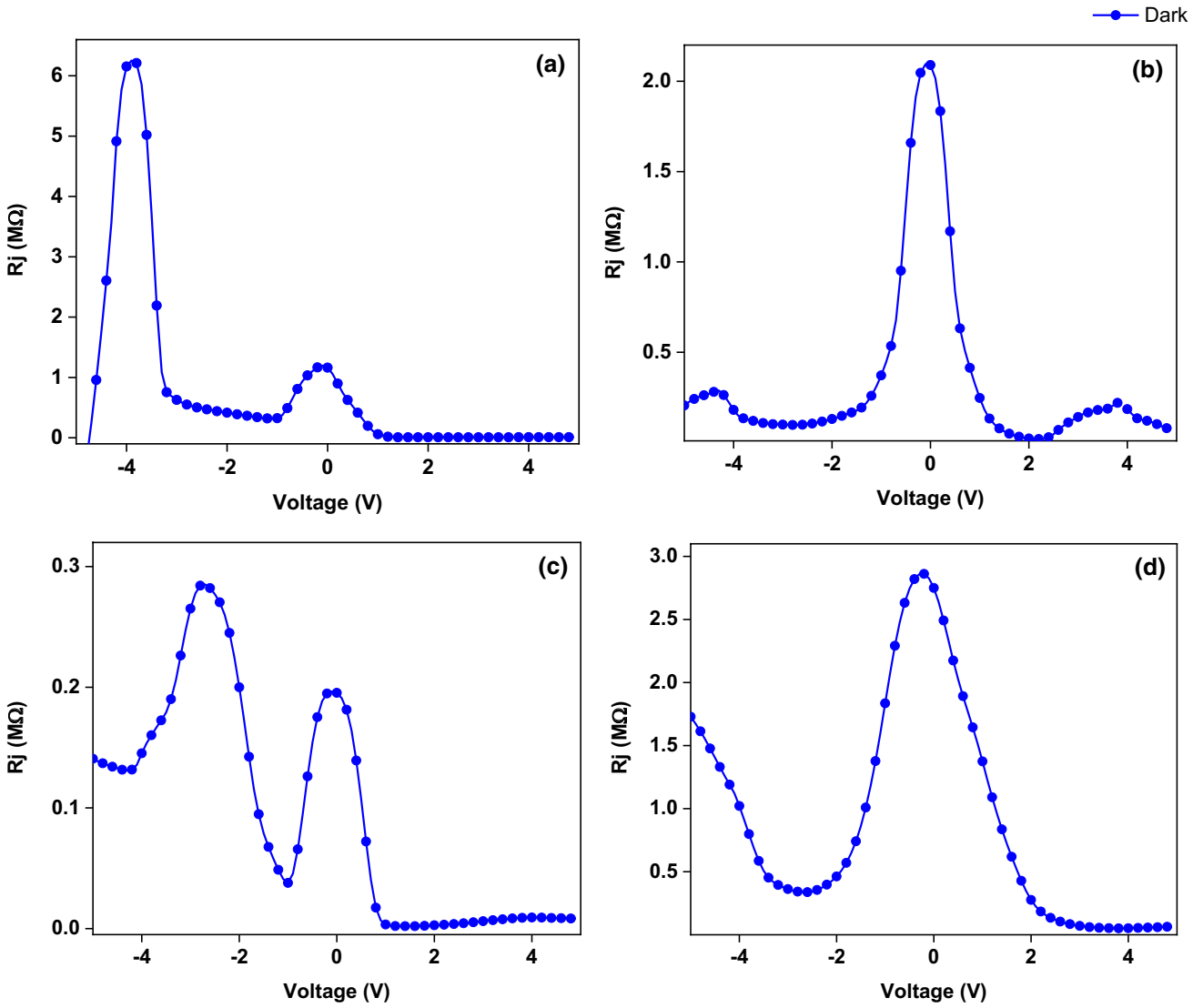

Fig. 7 R_j–V characteristics of the various Au-doped CuO interlayered Al/Au:CuO/*n*-Si heterostructures. (a) Undoped, (b) 1% Au doping, (c) 2% Au doping, and (d) 4% Au doping.

they can be employed for photodetector applications.[38,39] In this study, Au was used at various doping levels into CuO, and performance of the Al/Au:CuO/*n*-Si heterostructure against light was studied.

Various diode parameters such as ideality factor, series resistance, and barrier height values can be calculated by various techniques.[40–42] Thermionic emission theory can help to determine or calculate the saturation current, ideality factor, and barrier height of the various Au-doped Al/Au:CuO/*n*-Si heterostructures, and the obtained values are listed in Table IV. While saturation current (I_0) values increased with Au doping level, the barrier height values decreased according to undoped CuO interfacial layered heterostructure. The ideality factor values fluctuate with changing Au doping level. This fluctuation can be ascribed to the measurement errors or nonuniform interfacial CuO layer.[43]

Rectifying ratio (*RR*) plots of the various Au-doped CuO interlayered Al/Au:CuO/*n*-Si heterostructures are illustrated in Fig. 6 for increasing light power density. The highest *RR* value was obtained for pure the CuO interlayered Al/Au:CuO/*n*-Si heterostructure in dark condition. The *RR* values of the undoped and 1% Au-doped Al/Au:CuO/*n*-Si heterostructure decreased 20 mW/cm^2 light power density and stayed constant up to higher light power densities. In the case of higher Au doping level, the *RR* values stayed constant or slightly changed for changing light power density. These changes at the *RR* values can be attributed to the

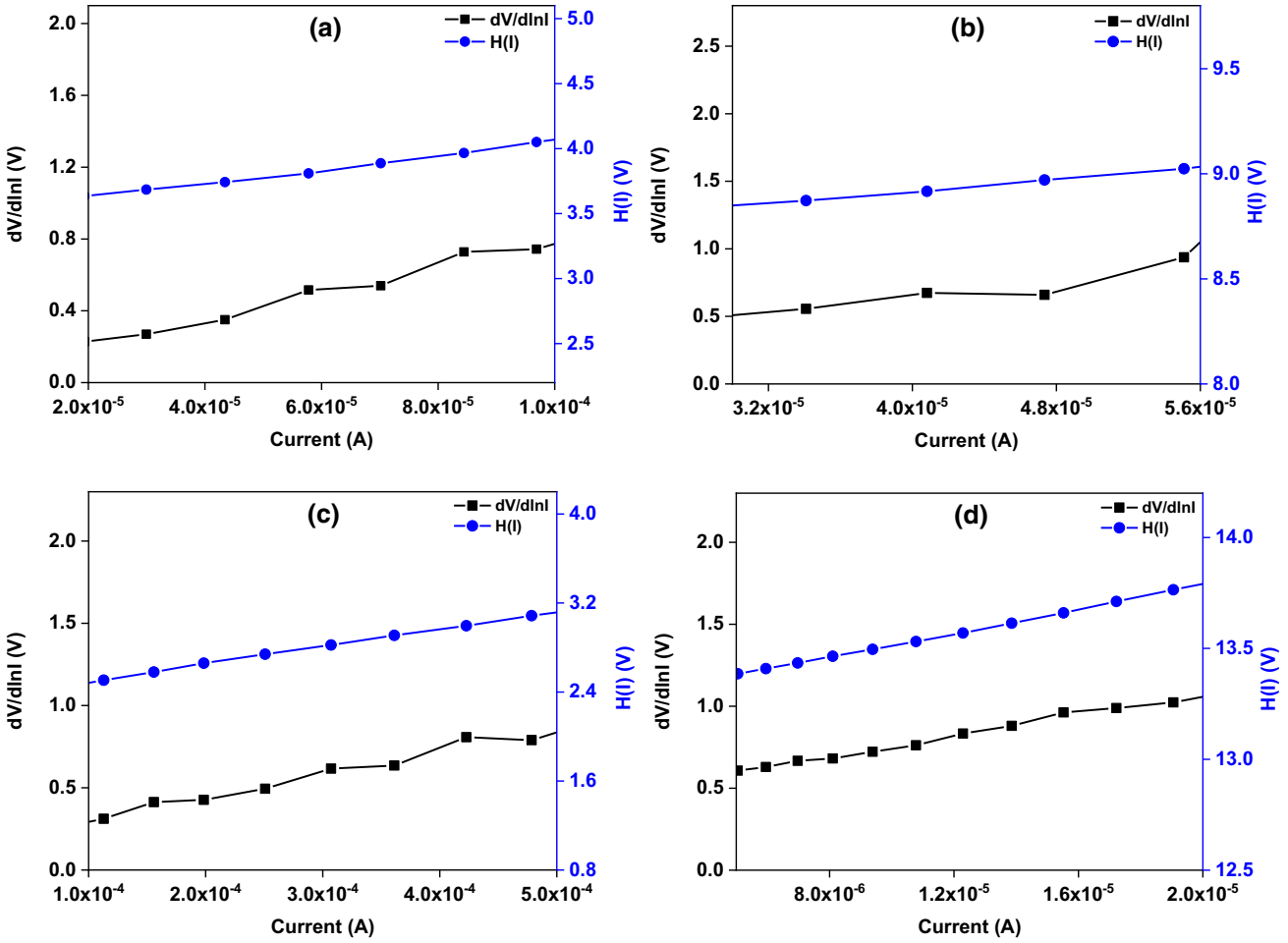

Fig. 8 Cheung plots of the various Au-doped CuO interlayered Al/Au:CuO/*n*-Si heterostructures. (a) Undoped, (b) 1% Au doping, (c) 2% Au doping-, and (d) 4% Au doping.

increasing Au doping which causes an increase of reverse current with increasing voltage.

The junction resistance (R_j) of the various Au-doped Al/Au:CuO/*n*-Si heterostructures are shown in Fig. 7. The R_j values generally have a series resistance (R_s) part at forward biases and a shunt resistance (R_{sh}) at reverse biases. These regions are clearly observed for all Au-doped Al/Au:CuO/*n*-Si heterostructures. All devices have a peak at around the 0 bias regions. The shunt resistance values decreased after Au doping to the CuO interlayer. However, the obtained shunt resistance values are at about 10^6 Ω for all heterostructures. The series resistance values fluctuate depending on the Au doping level.

The Cheung method can provide a way to calculate various diode parameters by plotting Cheung functions of d*V*/dln*I* and H(*I*) versus current.[44] Figure 8a, b, c, and d exhibit Cheung function plots for various Au doping levels. All the Al/Au:CuO/*n*-Si heterostructures have a linear profile and appropriate d*V*/dln*I* and H(*I*) functions. The calculated diode parameters are tabulated in Table IV for various heterostructures. The determined ideality factor and barrier height values are in good agreement with the diode parameters which were calculated from thermionic emission theory. Furthermore, the calculated series resistance from the d*V*/dln*I* and H(*I*) functions exhibited good harmony each other and confirmed the accuracy of the Cheung functions due to having close slope.

The Norde functions (*F(V)*) also can help to determine series resistance and barrier height by plotting versus voltage.[45] Figure 9 shows the Norde function plots of the various Au-doped Al/Au:CuO/*n*-Si heterostructures. The heterostructures revealed a Norde function profile with some distortion due to an interfacial layer effect.[46] The calculated barrier height and series resistance values are listed in Table IV. There are some deviations from the calculated values of the thermionic emission and Cheung method due to the approximation differences.[47]

The current transient measurements (*I–t*) reveal the level of response to changing light power density of a detector. The light is turned on and off sequentially to observe and measure this response time. Figure 10 displays *I–t* plots for the various

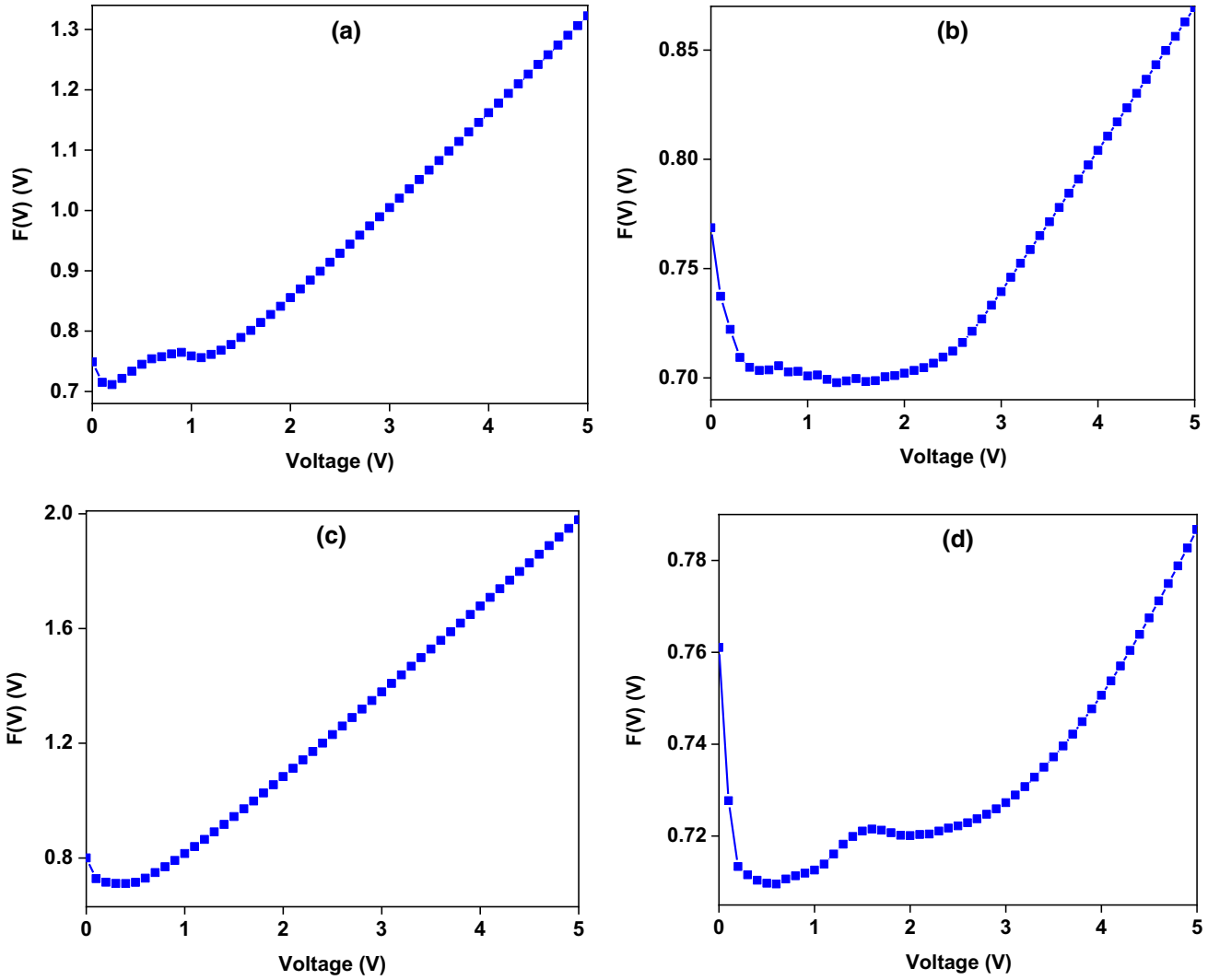

Fig. 9 Norde plots of the various Au-doped CuO interlayered Al/Au:CuO/*n*-Si heterostructures. (a) Undoped, (b) 1% Au doping, (c) 2% Au doping-, and (d) 4% Au doping-.

Au-doped Al/Au:CuO/*n*-Si heterostructures depending on the increasing light power illumination density. The current values increased almost linearly with increasing light power for each heterostructure. These results confirm the photoconductive behavior of the various Au-doped Al/Au:CuO/*n*-Si heterostructures.[48] However, the 2% Au-doped Al/Au:CuO/*n*-Si heterostructure has the highest current level.

The optical detector parameters of the various Au-doped CuO interlayered Al/Au:CuO/*n*-Si heterostructures are obtained by current transient characteristics. The photocurrent (I_p), photosensitivity (K), responsivity (R), and specific detectivity (D^*) values are calculated by the following equations, respectively:

$$I_p = I_{\text{light}} - I_{\text{dark}} \tag{5}$$

$$K = \frac{I_p}{I_{\text{dark}}} \tag{6}$$

$$R = \frac{I_p}{PA} \tag{7}$$

$$D^* = R\sqrt{\frac{A}{2qI_{\text{dark}}}} \tag{8}$$

where P is incident power density and A represents the effective detector area.

Table V displays the photodetector parameters depending on the increasing light power densities for the various Au-doped Al/Au:CuO/*n*-Si heterostructures. While the R and D^* values decreased with increasing light power density, the

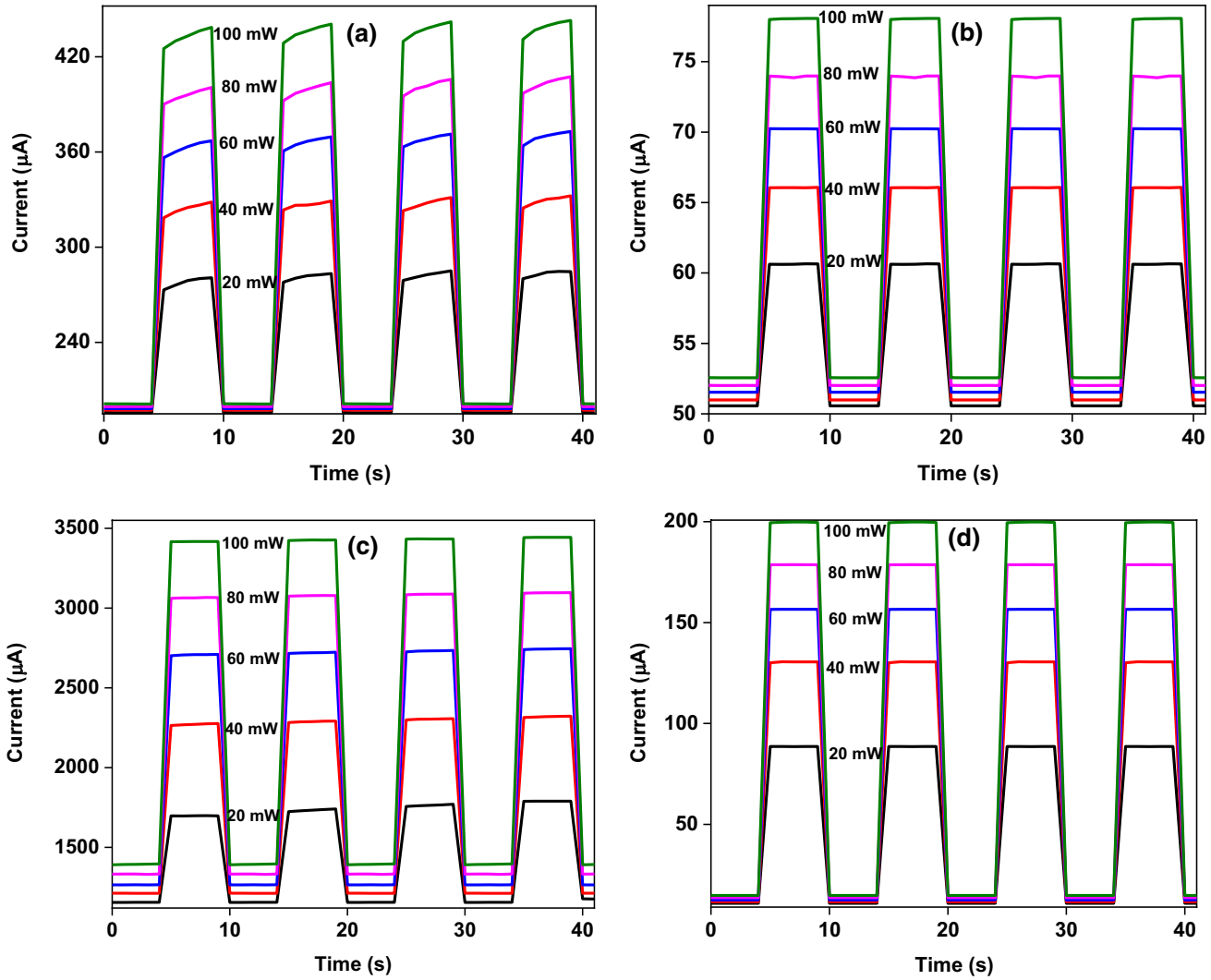

Fig. 10 *I–t* plots of the various Au-doped CuO interlayered Al/Au:CuO/*n*-Si heterostructures. (a) Undoped, (b) 1% Au doping, (c) 2% Au doping, and (d) 4% Au doping.

I_p and K values increased for all Au-doped Al/Au:CuO/*n*-Si heterostructures. The highest R values were obtained for the 2% Au-doped Al/Au:CuO/*n*-Si heterostructure, and the highest K and D^* values were calculated for the 4% Au-doped Al/Au:CuO/*n*-Si heterostructure. The Au-decorated heterostructures show better photodetection performance, and thus Au doping can be used to improve the photodetection performance of polymer or metal oxide interlayers.[49]

Conclusions

Copper oxide (CuO) thin films were fabricated using the cost-effective SILAR (successive ionic layer adsorption and reaction) technique, and their properties were investigated with respect to varying concentrations of gold (Au). The introduction of different levels of Au (0.00 M%, 1.0 M%, 2.0 M%, and 4.0 M%) had a notable impact on the structural, morphological, optical, and electrical characteristics of the CuO thin films. Adjusting the concentration of the doping agent played a significant role in modifying the crystalline structure and surface morphology of the films. The presence of Au led to a decrease in the crystallite size of the CuO thin films. SEM analysis revealed that the addition of Au to the growth solution resulted in distinct surface modifications in the CuO thin films. The optical bandgap energy of the films exhibited considerable sensitivity to the varying Au concentration, with bandgap values ranging between 1.45 eV and 1.52 eV. In conclusion, the outcomes of this study suggest that SILAR-deposited CuO thin films with varying Au concentrations possess a desirable range of optical transmittance and electrical conductivity, making them suitable for various

Table V Photodetector parameters for various Au-doped CuO interlayered Al/Au:CuO/*n*-Si of the heterostructures for various illumination densities

Au doping level	Power, mW/cm^2	Photocurrent, A	Photosensitivity	Responsivity, A/W	Specific detectivity, Jones
Undoped	20	8.32×10^{-5}	0.43	0.53	5.93×10^{9}
	40	1.28×10^{-4}	0.65	0.41	4.53×10^{9}
	60	1.65×10^{-4}	0.83	0.35	3.90×10^{9}
	80	1.96×10^{-4}	0.98	0.31	3.47×10^{9}
	100	2.32×10^{-4}	1.15	0.30	3.26×10^{9}
1%	20	1.00×10^{-5}	0.20	0.06	1.41×10^{9}
	40	1.51×10^{-5}	0.30	0.05	1.05×10^{9}
	60	1.87×10^{-5}	0.36	0.04	8.66×10^{8}
	80	2.19×10^{-5}	0.42	0.03	7.56×10^{8}
	100	2.55×10^{-5}	0.48	0.03	7.01×10^{8}
2%	20	5.40×10^{-4}	0.47	3.44	1.58×10^{10}
	40	1.05×10^{-3}	0.87	3.34	1.51×10^{10}
	60	1.43×10^{-3}	1.13	3.03	1.33×10^{10}
	80	1.73×10^{-3}	1.30	2.75	1.18×10^{10}
	100	2.03×10^{-3}	1.46	2.58	1.09×10^{10}
4%	20	7.76×10^{-5}	7.13	0.49	2.35×10^{10}
	40	1.19×10^{-4}	10.23	0.38	1.74×10^{10}
	60	1.44×10^{-4}	11.50	0.31	1.35×10^{10}
	80	1.65×10^{-4}	12.10	0.26	1.11×10^{10}
	100	1.85×10^{-4}	12.54	0.24	9.61×10^{9}

optoelectronic device applications. CuO films doped with varying amounts of Au were employed as the interlayer to fabricate Al/Au:CuO/*n*-Si heterostructures, which were characterized by *I–V* and *I–t* measurements for various power illumination densities. The Al/Au:CuO/*n*-Si heterostructures exhibited good photodiode behavior, with 3.44 A/W responsivity and 1.58×10^{10} Jones specific detectivity for 2% Au-doped CuO interfacial layer.

Acknowledgments This work was partially supported by the Selcuk University Scientific Research and Project Council (BAP) (Project No. BAP-21401015).

Author Contributions H.C.: Methodology, Project administration, Resources, Supervision, Validation, Visualization, Review & editing. A.A.H.: Review & editing, Writing—original draft, Data curation, Formal analysis. H.S.: Review & editing. A.K.: Conceptualization, Data curation, Investigation, Review & editing. F.D.: Writing–original draft, Review & editing. M.Y.: Project administration, Resources, Supervision, Validation, Visualization, Review & editing.

Data Availability The data that support the findings of this study are available from the corresponding author upon reasonable request.

Conflict of interest All authors declare that there are no potential conflicts of interest and that the study is not research involving human participants and/or animals.

References

1. Z. Bai and Y. Zhang, Self-powered UV–visible photodetectors based on ZnO/Cu2O nanowire/electrolyte heterojunctions. *J. Alloys Compd.* 675, 325 (2016).
2. M. Thirumoorthi, S. Shek Dhavud, V. Ganesh, T.H. Al Abdulaal, I.S. Yahia, and D. Deivatamil, High responsivity n-ZnO/p-CuO heterojunction thin film synthesised by low-cost SILAR method for photodiode applications. *Opt. Mater.* 128, 112410 (2022).
3. M. Tlili, C. Nefzi, B. Alhalaili, C. Bouzidi, L. Ajili, N. Jebbari, R. Vidu, and N.T. Kamoun, Synthesis and characterization of MgO thin films obtained by spray technique for optoelectronic applications. *Nanomaterials* 11, 3076 (2021).
4. M. Bouzbib, M. El Marouani, and K. Sinkó, Effect of various additives on aluminum oxide thin films prepared by dip coating, thermal behavior, kinetics and optical properties. *J. Eur. Opt. Soc. Rapid Publ.* 17, 25 (2021).
5. S.S. Parui, N. Kumar, P. Tiwari, N. Tiwari, and R.N. Chauhan, Zinc oxide and cupric oxide based thin films for solar cell applications. *Mater. Today Proc.* 41, 233 (2021).
6. H. Çavuşoğlu, Evaluating the influence of polyethylene glycol as a surfactant on CdO films grown by SILAR method. *J. Phys. Chem. Solids* 124, 67 (2019).
7. H. Cavusoglu, Exploring the role of pH on the physical and optoelectronic attributes of nanostructured NiO thin films. *J. Nanoelectron. Optoelectron.* 14, 645 (2019).
8. H. Cavusoglu, Band-gap control of nanostructured CuO thin films using PEG as a surfactant. *Eur. J. Sci. Technol.* 13, 124 (2018).
9. W. Maeng, S.H. Lee, J.D. Kwon, J. Park, and J.S. Park, Atomic layer deposited p-type copper oxide thin films and the associated thin film transistor properties. *Ceram. Int.* 42, 5517 (2016).

10. P.V. Raghavendra, J.S. Bhat, and N.G. Deshpande, Visible light sensitive cupric oxide metal-semiconductor-metal photodetectors. *Superlattices Microstruct.* 113, 754 (2018).
11. P. Horak, V. Bejsovec, J. Vacik, V. Lavrentiev, M. Vrnata, M. Kormunda, and S. Danis, Thin copper oxide films prepared by ion beam sputtering with subsequent thermal oxidation: Application in chemiresistors. *Appl. Surf. Sci.* 389, 751 (2016).
12. J. Zhang, Y. Zou, S. Eickelmann, C. Njel, H. Tobias, S. Ronneberger, V. Strauss, P.H. Seeberger, A. Savateev, and F.F. Loeffler, Laser-driven growth of structurally defined transition metal oxide nanocrystals on carbon nitride photoelectrodes in milliseconds. *Nat. Commun.* 12, 3224 (2021).
13. O. Gençyılmaz and T. Taşkopru, Effect of pH on the synthesis of CuO films by SILAR method. *J. Alloys Compd.* 695, 1205 (2017).
14. A.T. Carvalho, R.R. Lima, L.M. Silva, E. Fachini, and M.L.P. Silva, Nanostructured copper thin film used for catalysis. *Sens. Actuators B Chem.* 130, 141 (2008).
15. E.D. Jackson, J.M. Mosby, and A.L. Prieto, Evaluation of the electrochemical properties of crystalline copper antimonide thin film anodes for lithium ion batteries produced by single step electrodeposition. *Electrochim. Acta* 214, 253 (2016).
16. O.V. Diachenko, O.A. Dobrozhan, A.S. Opanasyuk, M.M. Ivashchenko, T.O. Protasova, D.I. Kurbatov, and A. Čerškus, The influence of optical and recombination losses on the efficiency of thin-film solar cells with a copper oxide absorber layer. *Superlattices Microstruct.* 122, 476 (2018).
17. R.L. Papurello, A.P. Cabello, M.A. Ulla, C.A. Neyertz, and J.M. Zamaro, Microreactor with copper oxide nanostructured films for catalytic gas phase oxidations. *Surf. Coat. Technol.* 328, 231 (2017).
18. C. Baratto, R. Kumar, G. Faglia, K. Vojisavljević, and B. Malič, p-Type copper aluminum oxide thin films for gas-sensing applications. *Sens. Actuators B Chem.* 209, 287 (2015).
19. D.M. Jundale, P.B. Joshi, S. Sen, and V.B. Patil, Nanocrystalline CuO thin films: synthesis, microstructural and optoelectronic properties. *J. Mater. Sci. Mater. Electron.* 23, 1492 (2012).
20. V. Saravanan, P. Shankar, G.K. Mani, and J.B.B. Rayappan, Growth and characterization of spray pyrolysis deposited copper oxide thin films: Influence of substrate and annealing temperatures. *J. Anal. Appl. Pyrolysis* 111, 272 (2015).
21. G. Qiu, S. Dharmarathna, Y. Zhang, N. Opembe, H. Huang, and S.L. Suib, Facile microwave-assisted hydrothermal synthesis of CuO nanomaterials and their catalytic and electrochemical properties. *J. Phys. Chem. C* 116, 468 (2012).
22. V. Dhanasekaran, T. Mahalingam, R. Chandramohan, J.K. Rhee, and J.P. Chu, Electrochemical deposition and characterization of cupric oxide thin films. *Thin Solid Films* 520, 6608 (2012).
23. V. Ramya, K. Neyvasagam, R. Chandramohan, S. Valanarasu, and A.M.F. Benial, Studies on chemical bath deposited CuO thin films for solar cells application. *J. Mater. Sci. Mater. Electron.* 26, 8489 (2015).
24. M.R. Das and P. Mitra, Influence of nickel incorporation on structural, optical and electrical characteristics of SILAR synthesized CuO thin films. *J. Solgel Sci. Technol.* 87, 59 (2018).
25. M. Amanullah, Q.A. Javed, and S. Rizwan, Surfactant-assisted carbon doping in ZnO nanowires using Poly Ethylene Glycol (PEG). *Mater. Chem. Phys.* 180, 128 (2016).
26. J. Zhang, K. Tse, M. Wong, Y. Zhang, and J. Zhu, A brief review of co-doping. *Front. Phys.* 11, 117405 (2016).
27. S. Zhang, The microscopic origin of the doping limits in semiconductors and wide-gap materials and recent developments in overcoming these limits a review. *J. Phys. Condens. Matter* 14, 881 (2002).
28. A. Abdel-Galil, N.L. Moussa, and I.S. Yahia, Study on spray deposited Ni-doped CuO nanostructured thin films: microstructural and optical behavior. *J. Mater. Sci. Mater. Electron.* 33, 4984 (2022).
29. Z.N. Kayani, W. Chaudhry, R. Sagheer, S. Riaz, and S. Naseem, Effect of Ce doping on crystallite size, band gap, dielectric and antibacterial properties of photocatalyst copper oxide Nano-structured thin films. *Mater. Sci. Eng.* 283, 115799 (2022).
30. A.A. Menazea and A.M. Mostafa, Ag doped CuO thin film prepared via pulsed laser deposition for 4-nitrophenol degradation. *J. Environ. Chem. Eng.* 8, 104104 (2020).
31. Md.M.H. Babu, J. Podder, R.R. Tofa, and L. Ali, Effect of Co doping in tailoring the crystallite size, surface morphology and optical band gap of CuO thin films prepared via thermal spray pyrolysis. *Surf. Interfaces* 25, 101269 (2021).
32. R. Aydin and H. Cavusoglu, Influence of sodium dodecyl sulfate as a surfactant on the microstructural, morphological and optoelectronic characteristics of SILAR deposited CuO thin films. *Mater. Res. Express* 6, 086403 (2019).
33. K.C. Preetha, K.V. Murali, A.J. Ragina, K. Deepa, and T.L. Remadevi, Studies on gold doped lead sulphide thin films grown by Silar technique. *AIP Conf. Proc.* 1391, 749 (2011).
34. M. Anwar, Z.N. Kayani, and A. Hassan, An insight of physical and antibacterial properties of Au-doped ZnO dip coated thin films. *Opt. Mater.* 118, 111276 (2021).
35. L. Ouarez, A. Chelouche, T. Touam, R. Mahiou, D. Djouadi, and A. Potdevin, Au-doped ZnO sol-gel thin films: An experimental investigation on physical and photoluminescence properties. *J. Lumin.* 203, 222 (2018).
36. R. Daira, A. Kabir, B. Boudjema, and C. Sedrati, Structural and optical transmittance analysis of CuO thin films deposited by the spray pyrolysis method. *Solid State Sci.* 104, 106254 (2020).
37. R.K. Pandey, K. Ghosh, S. Mishra, J.P. Bange, P.K. Bajpai, and D.K. Gautam, Effect of film thickness on structural and optical properties of sol-gel spin coated aluminum doped zinc oxide (Al:ZnO) thin films. *Mater. Res. Express.* 5, 086408 (2018).
38. N. Gogurla, A.K. Sinha, S. Santra, S. Manna, and S.K. Ray, Multifunctional Au-ZnO plasmonic nanostructures for enhanced UV photodetector and room temperature NO sensing devices. *Sci. Rep.* 4, 1 (2014).
39. H. Zhang, Y. Zhao, X. Geng, Y. Huang, Y. Li, H. Liu, Y. Liu, Y. Li, X. Wang, H. Tian, R. Liang, and T.L. Ren, Au nanoparticles-decorated surface Plasmon enhanced ZnO nanorods ultraviolet photodetector on flexible transparent mica substrate. *IEEE J. Electron. Devices Soc.* 7, 196 (2019).
40. A. Türüt, On current-voltage and capacitance-voltage characteristics of metal-semiconductor contacts. *Turkish J. Phys.* 44, 302 (2020).
41. M. Yilmaz, A. Kocyigit, B.B. Cirak, H. Kacus, U. Incekara, and S. Aydogan, The comparison of Co/hematoxylin/n-Si and Co/hematoxylin/p-Si devices as rectifier for a wide range temperature. *Mater. Sci. Semicond. Process.* 113, 105039 (2020).
42. D.E. Yıldız, H.H. Gullu, L. Toppare, and A. Cirpan, Analysis of temperature-dependent forward and leakage conduction mechanisms in organic thin film heterojunction diode with fluorine-based PCBM blend. *J. Mater. Sci. Mater. Electron.* 31, 15233 (2020).
43. A. Kocyigit, M. Yılmaz, Ş Aydoğan, and Ü. İncekara, The effect of measurements and layer coating homogeneity of AB on the Al/AB/p-Si devices. *J. Alloys Compd.* 790, 388 (2019).
44. S.K. Cheung and N.W. Cheung, Extraction of Schottky diode parameters from forward current-voltage characteristics. *Appl. Phys. Lett.* 49, 85 (1986).
45. H. Norde, A modified forward I-V plot for Schottky diodes with high series resistance. *J. Appl. Phys.* 50, 5052 (1979).
46. I. Missoum, Y.S. Ocak, M. Benhaliliba, C.E. Benouis, and A. Chaker, Microelectronic properties of organic Schottky diodes based on MgPc for solar cell applications. *Synth. Met.* 214, 76 (2016).
47. A. Kocyigit, M. Yilmaz, S. Aydogan, U. Incekara, and Y. Sahin, The performance of chitosan layer in Au/n-Si sandwich structures as a barrier modifier. *Polym. Test.* 89, 106546 (2020).

48. A. Mekki, R.O. Ocaya, A. Dere, A.A. Al-Ghamdi, K. Harrabi, and F. Yakuphanoglu, New photodiodes based graphene-organic semiconductor hybrid materials. *Synth. Met.* 213, 47 (2016).
49. H. Kacus, M. Yilmaz, U. Incekara, A. Kocyigit, and S. Aydogan, The photosensitive activity of organic/inorganic hybrid devices based on Aniline Blue dye: Au nanoparticles (AB@ Au NPs). *Sens. Actuators A Phys.* 15(330), 112856 (2021).